Simulation of a direct current microplasma discharge in helium at atmospheric pressure

Qiang Wang, Demetre J. Economou,[a) and Vincent M. Donnelly[b)
Plasma Processing Laboratory, Department of Chemical Engineering, University of Houston, Houston, Texas 77204-4004

A numerical simulation of a dc microplasma discharge in helium at atmospheric pressure was performed based on a one-dimensional fluid model. The microdischarge was found to resemble a macroscopic low pressure dc glow discharge in many respects. The simulation predicted the existence of electric field reversals in the negative glow under operating conditions that favor a high electron diffusion flux emanating from the cathode sheath. The electric field adjusts to satisfy continuity of the total current. Also, the electric field in the anode layer is self adjusted to be positive or negative to satisfy the "global" particle balance in the plasma. Gas heating was found to play an important role in shaping the electric field profiles both in the negative glow and the anode layer. Basic plasma properties such as electron temperature, electron density, gas temperature, and electric field were studied. Simulation results were in good agreement with experimental observations. © 2006 American Institute of Physics. [DOI: 10.1063/1.2214591]

I. INTRODUCTION

Microdischarges (or microplasmas) are characterized by their small size (characteristic dimensions, of tens to hundreds of microns) and high gas pressure (100 Torr – 1 atm), yielding nonequilibrium (cold) plasmas. There have been considerable efforts to develop microdischarge devices that can effectively generate and maintain stable discharges at such high pressures. These studies are motivated by numerous potential applications of microdischarges, including ultraviolet and vacuum ultraviolet light sources, sensors, microelectromechanical systems, and microreactors.[1–8] Modeling and simulation have also been carried out to understand the basic physics of microdischarges.[9–11] (Note that in the present context "microdischarges" refers to discharges under cw operation in contrast to pulsed dielectric barrier discharges.[11])

Microdischarges resemble the conventional low pressure, large-scale counterparts in many respects. In particular, both are nonequilibrium discharges, with an electron temperature much higher than the gas temperature (i.e., low-temperature plasmas). Nevertheless, microdischarges have several unique properties associated with their small dimension and high operating pressures. For example, increased collisionality at high pressure can cause a large fraction of the input power to be dissipated in gas heating. On the other hand, since microdischarges have a much larger surface-to-volume ratio in comparison with their large-scale counterparts, heat loss to the boundaries is quite efficient. As a result, the gas temperature in microdischarges can be only several hundreds of Kelvin above room temperature even at power densities of tens of $kW\,cm^{-3}$.[10,12] Moreover, three-body collisions such as atomic ion conversion to molecular ions and three-body quenching of excited states become important at high pressures.[13,14] Radiation trapping may also be significant for resonant radiation transitions at high gas pressures, but this effect may be counterbalanced by the small light path length within the microdischarge or become unimportant in comparison with three-body quenching processes.

In a recent publication,[12] spatially resolved measurements of several plasma properties in a direct current (dc) atmospheric pressure He microdischarge were presented, as well as successful comparisons of experimental data with results obtained from a fluid simulation. The aim of this work is to report the details of the simulation model (Sec. II) and to discuss additional microdischarge characteristics obtained from the simulation (Sec. III). In particular, electric field reversals in the negative glow, the polarity of the electric field in the anode layer, and the importance of gas heating will be discussed.

II. DESCRIPTION OF THE MODEL

A schematic of the parallel-plate microdischarge is shown in Fig. 1. A dc power supply (supplied voltage V) and a ballast resistor R_b are used to generate a microdischarge.
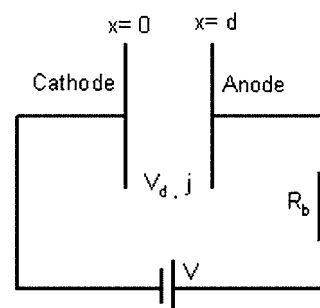
FIG. 1. Schematic of a one-dimensional parallel-plate microplasma with interelectrode spacing d powered by a dc power supply with voltage V. The microplasma source is in series with a ballast resistor, R_b. The discharge voltage is V_d and the discharge current density is j.

a)Electronic mail:economou@uh.edu
b)Electronic mail:vmdonnelly@uh.edu

The discharge voltage V_d is equal to the voltage difference between the two electrodes. The model was set up based on the well-known fluid approach.[15,16] The governing equations included transport of charged and neutral species, and Poisson's equation for the electric field. The basic assumptions of the model are as follows.

(1) The microdischarge properties are assumed to change only along the direction perpendicular to the electrodes so that a one-dimensional simulation is adequate.
(2) The charged particle flux is described by the drift/diffusion approximation.
(3) The electron energy distribution function (EEDF) is assumed Maxwellian and an equation for the electron temperature is solved.
(4) The temperature of ions and excited neutral species is assumed to equal the gas temperature.

The continuity equations for charged particles (including electrons, atomic ions, He^+, and molecular ions, He_2^+) are

$$\frac{\partial n_i}{\partial t} = - \nabla \cdot \mathbf{\Gamma_i} + S_i, \tag{1}$$

where n_i, $\mathbf{\Gamma_i}$, and S_i are the charged species number density, flux, and source function, respectively. S_i is a summation over the gas-phase reactions (see Table I) that produce or destroy charged particles. With the drift-diffusion approximation, the flux term is given by

$$\mathbf{\Gamma_i} = - D_i \nabla n_i \pm \mu_i \mathbf{E} n_i, \tag{2}$$

where D_i, μ_i, and $\mathbf{E}$ are the charged species diffusivity, mobility, and electric field, respectively. The negative sign is used for electrons while the positive sign is applied for positive ions.

Poisson's equation provides the space charge electric field

$$\nabla^2 V = - \nabla \cdot \mathbf{E} = - \frac{e}{\varepsilon_0} \left(\sum_i z_i n_i \right), \tag{3}$$

where V, ε_0, e, and z_i are the electric potential, vacuum permittivity, elementary charge, and charge number, respectively.

The electron energy equation reads

$$\frac{\partial}{\partial t} \left(\frac{3}{2} k n_e T_e \right) = - \nabla \cdot \mathbf{q_e} + \mathbf{j_e} \cdot \mathbf{E} + \sum_j R_{je} \Delta H_j + Q_{en} \tag{4}$$

with

$$\mathbf{q_e} = - K_e \nabla T_e + \frac{5}{2} k T_e \mathbf{\Gamma_e}, \tag{5}$$

where k is the Boltzmann constant, n_e is the electron density, T_e is the electron temperature, and $\mathbf{q_e}$ is the electron energy flux. $K_e [=(3/2)k D_e n_e]$ is the electron thermal conductivity and $\mathbf{\Gamma_e}$ is the electron flux. $\mathbf{j_e} = (e \mathbf{\Gamma_e})$ is the electron current density and $\mathbf{j_e} \cdot \mathbf{E}$ represents the electron Joule heating. The third and fourth terms on the right hand side of Eq. (4) represent electron energy gain and loss due to inelastic and elastic collisions, respectively. R_{je} is the rate coefficient for in-

elastic collisions of electrons with species j and ΔH_j is the corresponding energy exchange. Q_{en} is given by

$$Q_{en} = - 3 \frac{m_e}{M} n_e \nu_{en} (T_e - T_g), \tag{6}$$

where m_e, M, ν_{en}, and T_g are the electron mass, gas species mass, electron-neutral momentum transfer frequency, and gas temperature, respectively. The electron energy loss due to elastic electron-ion and electron-metastable collisions is neglected in the model due to the relatively low density of ions and metastables compared to the gas density. Use of Eq. (4) avoids the "local field" approximation may not be applicable under the strong cathode sheath electric field.

Three metastable states, including atomic metastables $[He(2\,^3S)$ and $He(2\,^1S)]$ and molecular metastable $[He_2(a\,^3\Sigma_u)]$, as well as the lowest atomic radiative state $[He(2\,^3P)]$ are considered in the model. The continuity equation for each of these four species reads

$$\frac{\partial n_m}{\partial t} = - \nabla \cdot (D_m \nabla n_m) + S_m, \tag{7}$$

where n_m is the species density, D_m is the diffusivity, and S_m is the source function that includes terms for the production and loss of metastables (or of the radiative state).

The $He(2\,^3P)$ state decays to $He(2\,^3S)$ by radiation. In the mass balances for $He(2\,^3P)$ and $He(2\,^3S)$ the radiation trapping effect is taken into account by multiplying $1/\tau$ (τ is the radiative lifetime) by an escape factor g (see Table I, R26). The escape factor g is usually given as a function of k_0 and L, where k_0 is the absorption coefficient at the center wavelength of the transition and L is the characteristic length. Since pressure broadening is the dominant broadening mechanism, k_0 is estimated by[17]

$$k_0 = \frac{\lambda_0^2 N'}{2\pi} \frac{g_2}{g_1} \frac{\gamma}{\gamma_p}, \tag{8}$$

where λ_0 is the central wavelength of the transition, N' is the number density of the absorber state [i.e, $He(2\,^3S)$], and g_1 and g_2 are the degeneracies of the lower and upper states, respectively, $\gamma = 1/\tau$ is the reciprocal of the lifetime of the upper excited state and γ_p represents a collisional frequency of the upper excited atoms with disturbing atoms (i.e., pressure broadening by He atoms) and is given in Ref. 18. Using Eq. (8), the corresponding opacity $k_0 L$ was estimated to be ~ 10. Therefore, the analytical formula for g, given in Ref. 19, which is suitable for a large opacity range ($0 < k_0 L < 1000$), was used.

A heat transport equation was employed to obtain the gas temperature T_g

$$\rho c_p \frac{\partial T_g}{\partial t} = \nabla \cdot (\lambda_g \nabla T_g) + P_g, \tag{9}$$

where c_p is the specific heat, λ_g is the thermal conductivity of the gas, and P_g is the power density dissipated as gas heating. Ion Joule heating (i.e., $\mathbf{j_+} \cdot \mathbf{E}$) and energy transfer during elastic electron-neutral collisions were considered to

contribute to P_g (see discussion in Sec. III). The gas number density N was obtained from the idea-gas law with the assumption of constant pressure.

A simple circuit model was employed to provide the discharge voltage V_d (used as boundary condition for Poisson's equation) given the ballast resistor and the power supply voltage.

$$V = V_d + jAR_b, \tag{10}$$

where j is the discharge current, self-consistently obtained during the calculation, and A is the area of each electrode.

Depending on the direction of the electric field at the electrode, the boundary conditions for charged species can

TABLE I. Reaction set included in the model.

No.	Reactions	Rate coefficient[a]	Reference
		Electron impact processes	
R1	$e + \text{He} \rightarrow \text{He} + e$	[b]	23
R2[c]	$e + \text{He} \rightarrow \text{He}^* + e$	[b]	24 and 25
R3	$e + \text{He} \rightarrow \text{He}^+ + e + e$	[b]	24 and 25
R4	$e + \text{He}(2\,^3S) \rightarrow \text{He}(2\,^1S) + e$	[b]	24
R5	$e + \text{He}(2\,^3S) \rightarrow \text{He}(2\,^3P) + e$	[b]	24
R6	$e + \text{He}(2\,^1S) \rightarrow \text{He}(2\,^3P) + e$	[b]	24
R7[c]	$e + \text{He}^* \rightarrow \text{He}^+ + e + e$	[b]	24
R8	$e + \text{He}(2\,^3P) \rightarrow \text{He}(2\,^1S) + e$	[b]	[d]
R9	$e + \text{He}(2\,^3P) \rightarrow \text{He}(2\,^3S) + e$	[b]	[d]
R10	$e + \text{He}(2\,^1S) \rightarrow \text{He}(2\,^3S) + e$	[b]	[d]
R11[c]	$e + \text{He}^* \rightarrow \text{He} + e$	[b]	[d]
R12[c]	$e + \text{He}_2^* \rightarrow \text{He}_2^+ + e + e$	$9.75 \times 10^{-10} T_e^{0.71} \exp(-3.4/T_e)$	26
R13[c]	$e + \text{He}_2^* \rightarrow \text{He} + \text{He} + e$	3.8×10^{-9}	23
R14[c]	$e + e + \text{He}^+ \rightarrow \text{He}^* + e$	$6.0 \times 10^{-20} (T_e/T_g)^{-4.4}$ cm^6 s^{-1}	23[e]
R15[c]	$e + \text{He} + \text{He}^+ \rightarrow \text{He}^* + \text{He}$	$1.0 \times 10^{-26} (T_e/T_g)^{-2.0}$ cm^6 s^{-1}	14[e]
R16[c]	$e + e + \text{He}_2^+ \rightarrow \text{He}(2\,^3P) + \text{He} + e$ $\rightarrow \text{He}_2^{**} + e$	$4.0 \times 10^{-20} (T_e/T_g)^{-1}$ cm^6 s^{-1}	23[f]
R17[c]	$e + \text{He} + \text{He}_2^+ \rightarrow \text{He}(2\,^3P) + 2\text{He}$ $\rightarrow \text{He}_2^{**} + \text{He}$	$5.0 \times 10^{-27} (T_e/T_g)^{-1}$ cm^6 s^{-1}	23[f]
R18[c]	$e + \text{He}_2^+ \rightarrow \text{He}_2^*$	$5.0 \times 10^{-9} (T_e/T_g)^{-1}$	24
		Heavy particle reactions	
R19[c]	$\text{He}^* + \text{He}^* \xrightarrow{x} \text{He}^+ + \text{He} + e$ $\xrightarrow{1-x} \text{He}_2^+ + e$	$2.9 \times 10^{-9} (T_g/0.025)^{0.5} (x=0.3)$	23 and 24
R20[c]	$\text{He}^* + \text{He}_2^* \xrightarrow{x} \text{He}^+ + 2\text{He} + e$ $\xrightarrow{1-x} \text{He}_2^+ + \text{He} + e$	$2.9 \times 10^{-9} (T_g/0.025)^{0.5} (x=0.3)$	23 and 24
R21[c]	$\text{He}_2^* + \text{He}_2^* \xrightarrow{x} \text{He}^+ + 3\text{He} + e$ $\xrightarrow{1-x} \text{He}_2^+ + 2\text{He} + e$	$2.9 \times 10^{-9} (T_g/0.025)^{0.5} (x=0.3)$	23 and 24
R22	$\text{He}^+ + \text{He} + \text{He} \rightarrow \text{He}_2^+ + \text{He}$	$1.4 \times 10^{-31} (T_g/0.025)^{-0.6}$ cm^6 s^{-1}	24
R23[c]	$\text{He}(2\,^3S) + \text{He} + \text{He} \rightarrow \text{He}_2^* + \text{He}$	$8.1 \times 10^{-36} T_g' \exp(-650/T_g')$ cm^6 s^{-1}	23 and 27
R24[c]	$\text{He}(2\,^1S) + \text{He} + \text{He} \rightarrow \text{He}_2^{**} + \text{He}$	1.3×10^{-33} cm^6 s^{-1}	14[g]
R25[c]	$\text{He}(2\,^3P) + \text{He} + \text{He} \rightarrow \text{He}_2^* + \text{He}$	1.6×10^{-32} cm^6 s^{-1}	14[g]
		Radiative transitions	
R26	$\text{He}(2\,^3P) \rightarrow \text{He}(2\,^3S) + h\nu$	$g(1.02 \times 10^7$ s$^{-1})$	14[h]

[a]Rate coefficients are in cm^3 s^{-1} unless noted otherwise, T_e is the electron temperature in V, T_g is the gas temperature in V, and T_g' is the gas temperature in K.
[b]Rate coefficients were determined from cross section data in the given reference, with the assumption of Maxwellian electron energy distribution.
[c]He* represents one of three atomic excited states, He($2\,^3S$), He($2\,^1S$), or He($2\,^3P$), He$_2^*$ represents the molecular metastable He$_2(a^3\Sigma_u)$, and He$_2^{**}$ represents the molecular radiative states.
[d]Rate coefficients obtained by detailed balance.
[e]The relative populations of He* were assumed to be according to their statistical weights.
[f]The relative populations of He($2\,^3S$) and He$_2^{**}$ were estimated as suggested in Ref. 13.
[g]Temperature dependence as suggested in Ref. 27.
[h]g is the radiation trapping factor mentioned in Sec. II.

TABLE II. Transport parameters for charged and neutral species.

Symbol	Description[a]	Values[b]	Reference
μ_e	Electron mobility	$2.83 \times 10^{22}/N$ cm^2 s^{-1} V^{-1}	21
D_e	Electron diffusivity	$(2.83 \times 10^{22}/N)T_e$ cm^2 s^{-1}	c
μ_+	He$^+$ mobility	$3.25 \times 10^{20}/N$ cm^2 s^{-1} V^{-1}	28
D_+	He$^+$ diffusivity	$(3.25 \times 10^{20}/N)T_g$ cm^2 s^{-1}	c,d
$\mu_+{}'$	He$_2^+$ mobility	$4.88 \times 10^{20}/N$ cm^2 s^{-1} V^{-1}	28
$D_+{}'$	He$_2^+$ diffusivity	$(4.88 \times 10^{20}/N)T_g$ cm^2 s^{-1}	c,d
D_{m1}	He* diffusivity[b]	$(420/p) \times (T_g/0.025)^{1.5}$ cm^2 s^{-1}	23 and 24
D_{m2}	He$_2{}^*$ diffusivity	$(305/p) \times (T_g/0.025)^{1.5}$ cm^2 s^{-1}	23 and 24[e]
λ_g	He thermal conductivity	$7.22 \times 10^{-4} + 2.84 \times 10^{-6} T_g{}'$	29
		$-5.25 \times 10^{-11} T_g{}'^2$ J cm^{-1} s^{-1} K^{-1}	29

[a]He* represents one of three atomic excited states He(2 ^3S), He(2 ^1S), or He(2 ^3P), and He$_2{}^*$ represents the molecular metastable He$_2(a\ ^3\Sigma_u)$.

[b]N is the gas number density in cm^{-3}, T_e is the electron temperate in V, T_g is gas temperature in V, p is gas pressure in Torr, and $T_g{}'$ is gas temperature in K.

[c]Assumed to follow Einstein's relation.

[d]The ion and excited neutral species temperature was assumed to equal the gas temperature.

[e]Temperature dependence as suggested in Ref. 24.

be different.[20] A general expression is given by introducing a parameter a, which is set equal to unity if the electric field is directed towards the electrode, and zero otherwise. The corresponding boundary condition for electrons at the cathode ($x=0$) or the anode ($x=d$) reads,

$$\mathbf{\Gamma_e} = \frac{1}{4} v_{\text{th}}{}^e n_e \hat{\mathbf{n}} - a\gamma_+ \mathbf{\Gamma}_+ + (a-1)\mu_e \mathbf{E} n_e \quad \text{at } x=0,d, \quad (11)$$

where $v_{\text{th}}{}^e = (8kT_e/\pi m_e)^{1/2}$ is the electron thermal velocity, $\hat{\mathbf{n}}$ is the normal vector pointing outwards, and γ_+ is the secondary electron emission coefficient for ions. The corresponding boundary condition for positive ions is given by

$$\mathbf{\Gamma}_+ = \frac{1}{4} n_+ v_{\text{th}}{}^+ \hat{\mathbf{n}} + a\mu_+ \mathbf{E} n_+ \quad \text{at } x=0,d, \quad (12)$$

where $\mathbf{\Gamma}_+$ is the ion flux and $v_{\text{th}}{}^+ = (8kT_g/\pi M)^{1/2}$ is the ion thermal velocity. In Eqs. (11) and (12), if the electric field is directed towards the electrode ($a=1$), the electron flux equals the thermal flux minus the secondary electron emission flux, while the ion flux equals the ion thermal flux plus the ion drift flux. Note that due to the low mobility of ions at atmospheric pressure, the ion thermal flux can be of the same order of magnitude as the ion drift flux when the electric field strength at the electrode is below some 10 kV cm^{-1}. On the other hand, if the electric field is directed away from the electrode ($a=0$), the electron flux equals the electron thermal flux plus the electron drift flux, while the ion flux equals the ion thermal flux. For the dc glow discharges of interest here, the cathode sheath electric field is always directed towards the cathode, whereas the anode sheath field can be directed either towards or away from the anode.[21](See discussion in Sec. III.)

The boundary condition for electron temperature is written in the form of an energy balance at the electrode,[16]

$$\mathbf{q_e} = \left(\frac{5}{2}kT_e\right)\left[\frac{1}{4} n_e v_{\text{th}}{}^e \hat{\mathbf{n}} + (a-1)\mu_e \mathbf{E} n_e\right]$$
$$- a\left(\frac{5}{2}kT_{\text{se}}\right)\gamma_+ \mathbf{\Gamma}_+ \quad \text{at } x=0,d, \quad (13)$$

where T_{se} is the temperature of the secondary electrons ejected from the electrode ($T_{\text{se}} \approx 5$ eV for He$^+$ on Mo surface[22] and the same value was assumed for He$_2^+$).

The boundary condition for the neutral species is given by

$$\mathbf{\Gamma_m} = \frac{1}{4} n_m v_{\text{th}}{}^m \hat{\mathbf{n}} \quad \text{at } x=0,d, \quad (14)$$

where $\mathbf{\Gamma_m}$ is the neutral species flux and $v_{\text{th}}{}^m = (8kT_g/\pi M)^{1/2}$ is the neutral species thermal velocity at the electrode.

The boundary condition on the electric potential (Possion's equation) was specified as $V=0$ on the cathode and $V=V_{\text{dis}}$ on the anode, where the discharge voltage V_{dis} was found as part of the solution and was adjusted during the simulation according to Eq. (10). Finally, the gas temperature at $x=0,d$ was assumed to be equal to the electrode temperature which was taken to be 350 K for both electrodes.

Table I lists the reactions that were taken into account in the model. For electron impact excitation and ionization (R1–R11), the rate coefficients were calculated from the known cross sections with the assumption of Maxwellian electrons. Look up tables were used to interpolate the rate coefficients. For reactions involving heavy particles, the rate coefficients were expressed, where possible, as a function of gas temperature.

Transport parameters of charged and neutral species are listed in Table II as a function of gas density and/or gas temperature. The reduced mobility of charged species $\mu_e N$ and $\mu_+ N$ was assumed to be constant, and the reduced diffusivity $D_e N$ and $D_+ N$ was assumed to follow Einstein's rela-
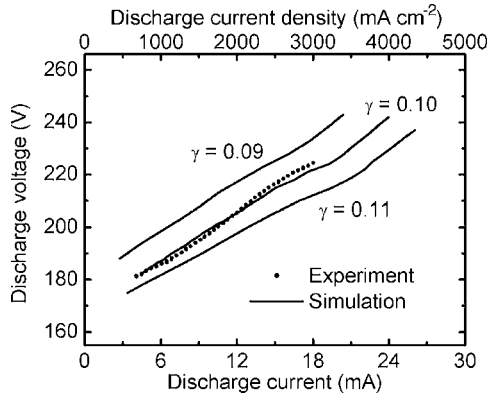
FIG. 2. Simulated (lines) current-voltage (*I-V*) characteristics in a parallel-plate helium dc microdischarge. Experimental data (points) were taken from Ref. 12. The discharge pressure was 760 Torr and the interelectrode gap was 200 μm. The sensitivity of the simulated *I-V* to the secondary electron emission coefficient (by ion bombardment) γ is illustrated by curves with γ =0.09, 0.10, and 0.11, respectively.

tion. Thus, with the assumption of constant pressure, both mobility and diffusivity of charged species are proportional to the gas temperature.

The model equations [Eqs. (1), (3), (4), (7), (9), and (10)] were integrated simultaneously using a finite difference method on a "staggered mesh."[30] Charged species densities, neutral species densities, electron temperature, electric potential, and gas temperature were computed at the mid-distance between grid points, while flux terms were computed at the grid points. Spatial discretization of the equations resulted in a differential/algebraic equations (DAE) system, which was integrated in time using a backward difference formula[15] until a steady state was reached. Simulations used an equally spaced finite difference grid with 400 points.

III. RESULTS AND DISCUSSION

Figure 2 shows the comparison between calculated and experimental current-voltage (*I-V*) characteristics for a He dc microdischarge at atmospheric pressure, with a 200 μm interelectrode gap and a ballast resistor of 10 kΩ. (Detailed description of the experiments can be found in Ref. 12.) The calculated *I-V* characteristic is sensitive to the secondary electron emission coefficient γ. Model predictions agree best with the data for γ=0.10. The positive slope of the *I-V* characteristic is an indication that the discharge operates in the abnormal glow regime.[21] Comparison of simulation predictions and experimental measurements of electron density, cathode sheath electric field, and gas temperature as a function of position in the gap was presented in Ref. 12.

Table III lists the parameter values used for the three cases discussed in this paper. The base case (case 1) values are for a discharge current density of approximately 3600 mA cm^{-2}. Case 2 and case 3 are for a lower current density or a larger gap, respectively. Results shown below are for steady-state discharges.

A. Basic plasma properties

Figure 3 presents simulation results of several basic plasma properties, including the electric potential, electron temperature, charged and excited neutral species densities, and ionization rates, for the base case (case 1). The potential profile [Fig. 3(a)] shows a very large voltage drop of ~232 V in the cathode fall. The corresponding electric field strength (not shown) peaks at the cathode (~96 kV cm^{-1}) and decays to very small values (<1 kV cm^{-1}) over a distance of ~55 μm from the cathode. The electric field in the negative glow and in the anode regions will be shown and discussed in the following.

The electron temperature distribution [Fig. 3(a)] shows a maximum of ~24 eV in the cathode sheath and decreases

TABLE III. Simulation input parameters and some simulation results

	Case 1	Case 2	Case 3
Simulation input parameters			
Gas pressure p (Torr)	760	760	760
Interelectrode spacing d (μm)	200	200	300
Ballast resistor R_b (kΩ)	10	10	10
Electrode surface area S (cm^2)	0.006	0.006	0.006
Applied dc voltage V (V)	449	240	460
Selected simulation results			
Discharge current density j (mA cm^{-2})	3601.6	903.3	3599.5
Discharge voltage V_d (V)	232.9	185.8	244.0
Cathode sheath thickness (μm)	57.0	76.6	58.7
Peak electron temperature (eV)	23.9	14.1	24.5
Peak gas temperature (K)	620	420	650
Bulk average electron temperature (eV)	1.1	1.0	1.0
Bulk average gas temperature (K)	520	390	560
Bulk average electron density (cm^{-3})	1.0×10^{14}	0.1×10^{14}	0.9×10^{14}
Number of electric field reversals in bulk plasma	1	0	2
Anode potential with respect to nearby space potential	Negative	Positive	Positive
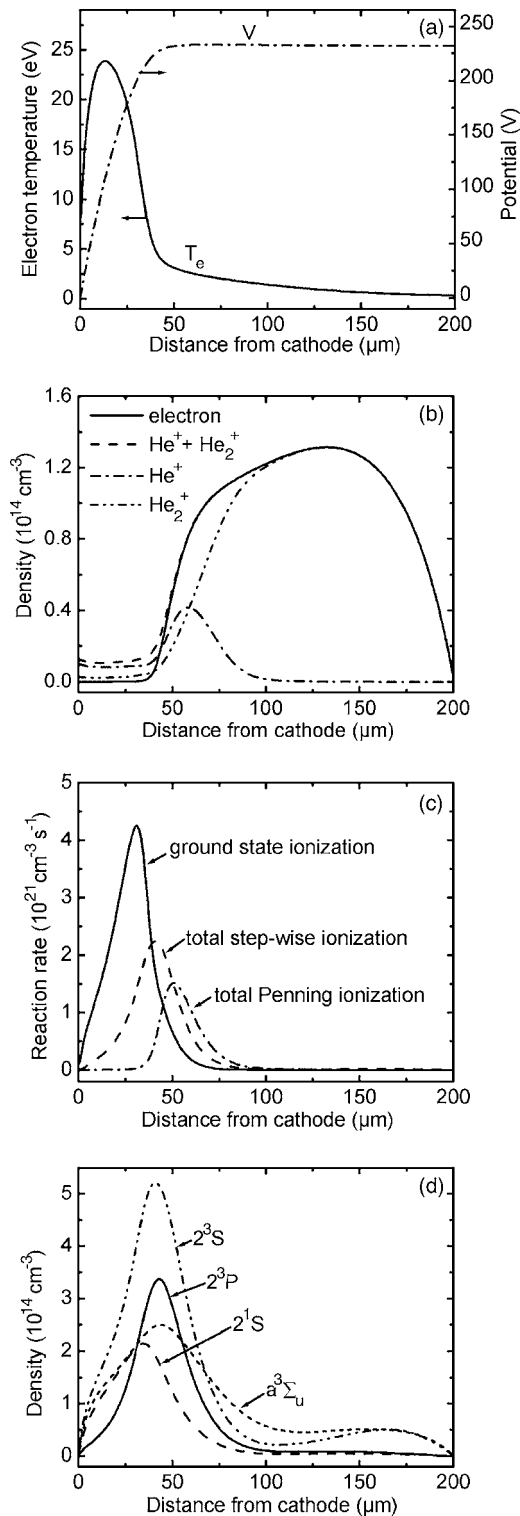
FIG. 3. Plasma properties for the base case (case 1 of Table III) as a function of position: (a) electric potential and electron temperature, (b) charged particle densities, including electron, He^+, He_2^+ and $He^+ + He_2^+$, (c) reaction rates for ground state ionization, total stepwise ionization, and Penning ionization, and (d) metastable densities, including $He(2\,^3S)$, $He(2\,^1S)$, $He_2(a\,^3\Sigma_u)$, and the radiative state $He(2\,^3P)$ density.

rapidly to much smaller values (~ 1 eV) in the negative glow. The high electron temperature in the cathode sheath is the result of Joule heating in the high electric field. In addition, Penning ionization (reactions R19–21 in Table I) with a

maximum reaction rate near the sheath edge (see Fig. 3(d)) can produce "hot" electrons with energy of ~ 15 eV.[23]

Figure 3(b) shows the charged species (i.e., e^-, He^+ and He_2^+) density distributions between the two electrodes. The electron density peaks in the negative glow at nearly 1.3 $\times 10^{14}$ cm^{-3}. The total ion density (i.e., $He^+ + He_2^+$) is only very slightly higher than the electron density in the negative glow where quasineutrality is maintained, while it dominates the electron density in the cathode sheath region. He^+ is the major ion species in the cathode sheath, while He_2^+, the result of ion conversion (reaction R22), is the dominant ion species in the negative glow and anode regions. Similar ion density profiles have been reported in previous simulations.[9]

The ionization rate profiles, including ground state ionization (R3), overall stepwise ionization (R7+R12) and total Penning ionization (R19+R20+R21) are shown in Fig. 3(c). Ground state ionization (R3) is the major electron production channel. It peaks in the cathode sheath near the electron temperature maximum. Among the stepwise ionization processes, ionization of the $2\,^3S$ state was found to be most important. For Penning ionization, the maximum reaction rate is located near the cathode sheath edge, where the metastable densities are highest [see Fig. 3(d)]. The most important Penning ionization was the reaction between $He(2\,^3S)$ states.

Figure 3(d) shows the density profiles of the excited neutral species [i.e., $He(2\,^3S)$, $He(2\,^1S)$, $He(2\,^3P)$, and $He_2(a\,^3\Sigma_u)$] that have been taken into account in the model. The density of all four states peaks near the cathode fall edge at $\sim 2 \times 10^{14} - 5 \times 10^{14}$ cm^{-3}. Reactions involving electron impact processes were found to be important for the three atomic excited states. For example, the $2\,^3S$ state is mainly created by ground state electron impact excitation and electron quenching from the $2\,^3P$ state and is mainly destroyed by reexcitation to the $2\,^3P$ state. The $2\,^3P$ state is generated mainly by stepwise excitation from the $2\,^1S$ state and is lost mainly by radiative decay and electron quenching. Diffusion was found not to be important for these excited states (the characteristic diffusion time is ~ 0.1 ms, while the characteristic reaction time is $\sim 0.1 - 1$ μs). The calculated escape factor g for the nonresonant transition $2\,^3P \rightarrow 2\,^3S$ was in the range $\sim 0.08 - 0.8$. The most intense radiation trapping (i.e., minimum value of g) occurs at the position where the metastable $2\,^3S$ density peaks. It was also found that the three-body metastable conversion (R23) and Penning ionization (R21) were the dominant creation and loss processes for the molecular metastable state, respectively.

In Eq. (9), the gas heating source function P_g was set equal to $\mathbf{j}_+ \cdot \mathbf{E} + Q_{en}$, where $\mathbf{j}_+ \cdot \mathbf{E}$ represents the ion Joule heating (i.e., energy transfer by collisions of ions with the background gas) and Q_{en} is the energy transferred due to elastic electron-neutral collisions. In order to analyze the contributions from different gas heating mechanisms, two more cases were examined: (case 1a) the power deposition into the gas was assumed to be by ion Joule heating alone (i.e., $P_g = \mathbf{j}_+ \cdot \mathbf{E}$) and (case 1b) the power deposition into the gas was assumed to be the total power input in the discharge (i.e., $P_g = \mathbf{j} \cdot \mathbf{E}$). The latter case would produce an upper limit for the gas temperature. Figure 4 shows the gas temperature pro-
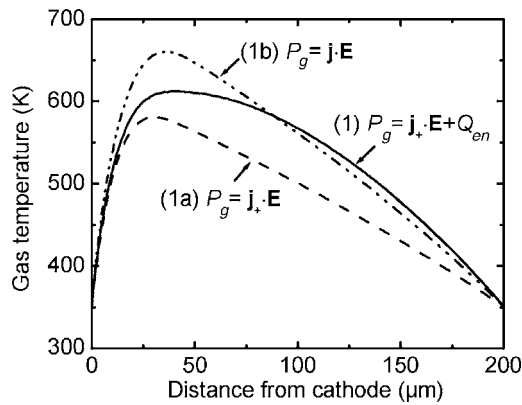
FIG. 4. Gas temperature profile as a function of position for case 1 (Table III), for three different gas heating mechanisms: (1) ion Joule heating and elastic electron-neutral collisions (i.e., $P_g = \mathbf{j}_+ \cdot \mathbf{E} + Q_{en}$), (1a) ion Joule heating only (i.e., $P_g = \mathbf{j}_+ \cdot \mathbf{E}$), and (1b) total power deposited into the discharge (i.e., $P_g = \mathbf{j} \cdot \mathbf{E}$).

files between the two electrodes for cases 1, 1a, and 1b. The predicted temperature profiles under the three cases are quite similar, suggesting that the dominant gas heating is ion Joule heating. In case 1, in fact, 82% of the total discharge power ends up heating the gas by ion Joule heating, while only 8% of the discharge power is dissipated in elastic electron-neutral collisions. In all three cases, the gas temperature peaks in the cathode sheath where the electric field is high. Positive ions gain energy from the field and collisionally transfer this energy to the neutral gas, thereby heating the gas. Other gas heating sources may include the energy released by heavy particle reactions.[10] However, their contribution was very small under these conditions and was thus ignored.

Microdischarge plasma properties as a function of the current density are shown in Fig. 5. For the range of current density investigated, the cathode sheath thickness decreases from ~120 μm at 260 mA cm^{-2} to ~56 μm at 4000 mA cm^{-2}. The sheath thickness was defined as the distance from the cathode where the net charge density divided by the positive ion density was 0.01. The peak electron temperature and gas temperature increase from 10 to 25 eV and from 370 to 650 K, respectively. The average electron density and gas temperature in the bulk also increase with current density [Fig. 5(b)]. In contract, the electron temperature in the bulk is quite low (~1 eV) and is insensitive to current density. The predicted gas temperature, electron density, and cathode sheath thickness have been shown to be in good agreement with experimental data.[12]

B. Electric field profiles in the bulk plasma region

Electric field reversals in the negative glow of low pressure dc discharges have been detected by laser optogalvanic spectroscopy and have been studied by analytical modeling and numerical simulation.[31,32] Do such field reversals also occur in high pressure microdischarges?

Figure 6 presents the calculated electric field profiles in the negative glow and anode regions for the relatively high (case 1) and low (case 2) current densities. For the high current density case, the simulation clearly predicts electric
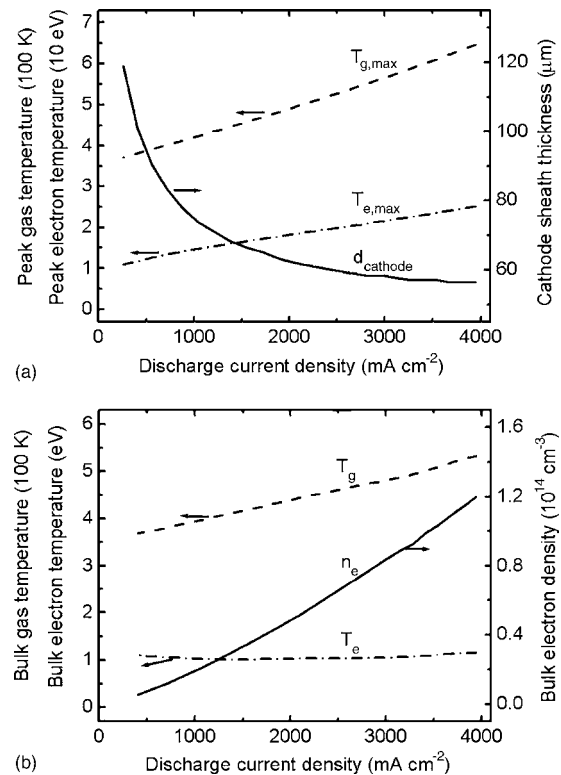
FIG. 5. Plasma properties for a He dc microdischarge at $p = 760$ Torr and $d = 200$ μm as a function of discharge current density: (a) peak gas temperature, peak electron temperature, and cathode sheath thickness and (b) bulk gas temperature, bulk electron temperature, and bulk electron density (spatially average values over the bulk plasma region, i.e., from the sheath edge to the anode. The sheath edge was defined as the position where the relative net charge ratio $(n_e - n_i)/n_i = 0.01$.

field reversal (the field changes from negative to positive) in the negative glow near the cathode sheath edge. This is indicated by an arrow in Fig. 6. The field profile for case 1 also shows a local maximum of the electric field on the anode side of the field reversal, indicating the existence of a charge double layer. This field profile resembles that shown in Ref. 31. In contrast, for the low current density case, the electric field is always negative, and field reversal does not occur. Besides different behaviors regarding field reversal, these two cases also show quite different features of the electric field in the anode region. This will be discussed in the next section.
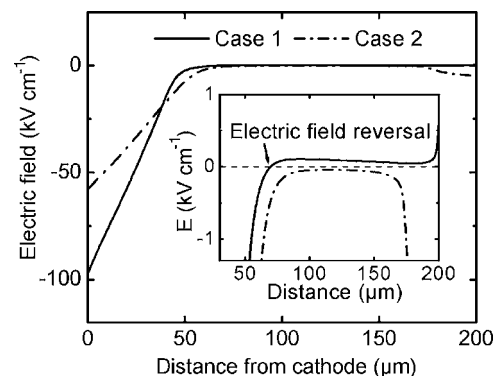
FIG. 6. Electric field profiles for the He dc microdischarges of case 1 and case 2. Insert shows the electric field in the bulk and anode regions, and the presence of an electric field reversal is indicated by the arrow.
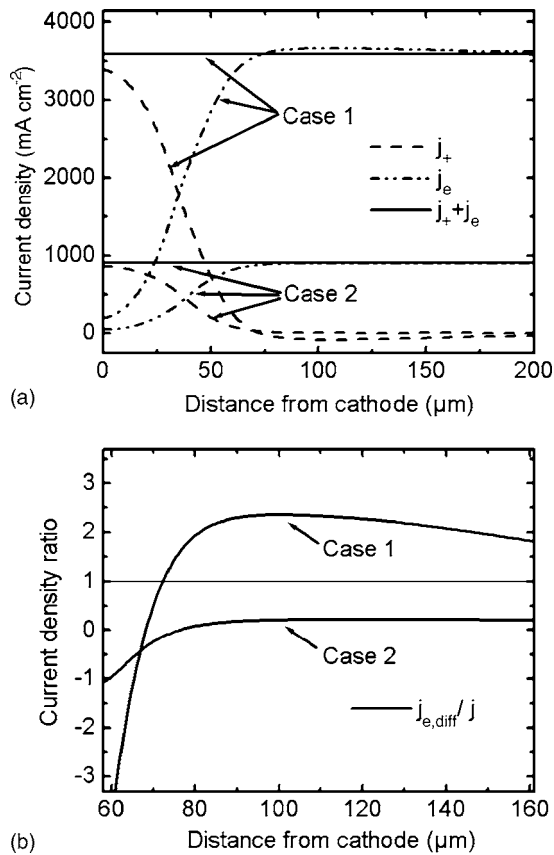
FIG. 7. Current density profiles for the He dc microdischarges of case 1 and case 2: (a) Ion current density j_+, electron current density j_e, and total discharge current density $j=j_++j_e$. (b) Current density ratio $j_{e,\mathrm{dif}}/j$ in the bulk region.

FIG. 8. Potential, electron density, and ion density in the anode layer of a He dc microdischarge at $p=760$ Torr and $d=200$ μm for (a) case 1 and (b) case 2.

The presence (or absence) of electric field reversal can be explained based on the conservation of discharge current. The calculated ion current density, j_+, electron current density j_e, and total current density j as a function of position between the electrodes are shown in Fig. 7(a). In both case 1 and case 2, the total discharge current remains independent of position, as expected. j_+ dominates j_e in the cathode fall. In the rest of the discharge, however, almost all current is carried by electrons. Because ions contribute negligible current in the negative glow and anode regions, the conservation of the discharge current in these regions can be expressed approximately as $j\approx j_e=j_{e,\mathrm{dif}}+j_{e,\mathrm{dri}}$, where $j_{e,\mathrm{dif}}$ and $j_{e,\mathrm{dri}}$ represent the electron current density due to diffusion and drift, respectively. Depending on the ratio between $j_{e,\mathrm{dif}}$ and j_e, the local electric field is self-adjusted to either constrain or enhance the electron drift current in order to maintain the total current constant.

Figure 7(b) presents the ratio $j_{e,\mathrm{dif}}/j$, outside the cathode fall, for cases 1 and 2. In the cathode fall, $j_{e,\mathrm{dif}}/j\ll 1$. For case 1 (high j), $j_{e,\mathrm{dif}}/j$ becomes larger than unity at a distance of $l\sim 72$ μm from the cathode, all the way to the anode. The turning point at $l\sim 72$ μm is in good agreement with the position of the electric field reversal shown in Fig. 6. For case 2 (low j), $j_{e,\mathrm{dif}}/j$ is always less than unity. As a result, the electric field is required to stay negative to enhance the electron drift and no field reversal occurs. In essence, the presence of a large electron diffusion current emanating from the sheath necessitates the formation of field reversal.

Gas heating was found to affect electric field reversal. In particular, when gas heating was not taken account (for example, by assuming $T_g=300$ K), $j_{e,\mathrm{dif}}/j$ was found to be less than unity throughout the discharge, and the electric field reversal did not occur under the conditions of case 1. When neglecting gas heating, field reversal occurred at even higher current density ($j>4800$ mA cm^{-2}). At this current density, the electron diffusion current from the sheath was large enough, for the electric field to change direction in order to conserve the total current.

C. Electric fields in the anode region

As shown in Fig. 6, the electric field in case 1 is directed towards the anode (it is positive) and the field strength increases as the anode is approached. The corresponding anode potential is slightly below the nearby space potential forming a small (positive ion) anode sheath [Fig. 8(a)]. In case 2, the electric field is directed away from the anode (it is negative, see Fig. 6) and the corresponding anode potential floats above the nearby space potential. Electrons dominate positive ions in the anode layer, indicating the formation of an electron anode sheath [Fig. 8(b)]. Similar behavior of the electric field in the anode layer has been mentioned in low pressure dc glow discharges.[21] Under what conditions is the electric field at the anode positive or negative?
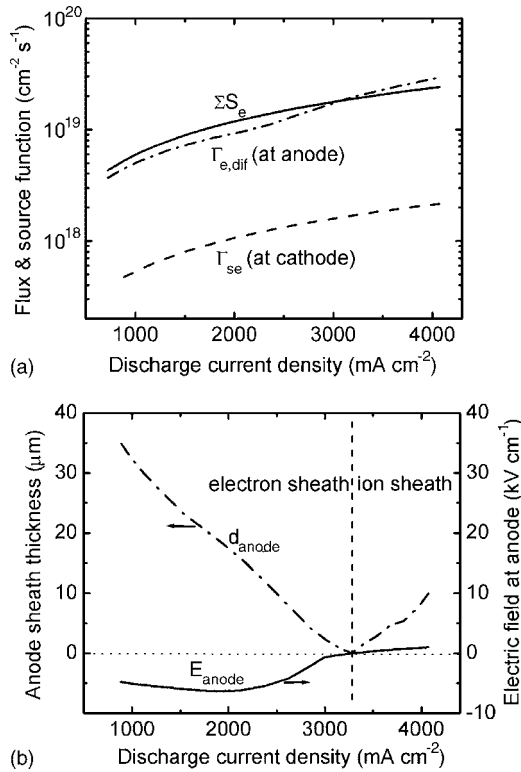
FIG. 9. Plasma properties for He dc microdischarges at $p=760$ Torr and $d=200$ μm as a function of discharge current density: (a) secondary electron flux at the cathode, electron diffusion flux at the anode, and spatially integrated electron source function, and (b) anode sheath thickness and electric field at the anode. [The anode sheath edge was defined as the position where the relative net charge $(n_e-n_i)/n_i=0.01$.]

At steady state, the overall electron generation rate must equal the electron loss rate. Since electron loss at the boundaries dominates,

$$\sum S_e + \Gamma_{se}{}^C = \Gamma_e{}^A, \tag{15}$$

where ΣS_e represents the space integrated electron source function, $\Gamma_{se}{}^C$ represents the secondary electron flux at the cathode (note that the electron diffusion loss to the cathode is negligible), and $\Gamma_e{}^A$ $(=\Gamma_{e,\mathrm{dif}}{}^A+\Gamma_{e,\mathrm{dri}}{}^A)$ is the electron flux at the anode, including a diffusion component $\Gamma_{e,\mathrm{dif}}{}^A$ and a drift component $\Gamma_{e,\mathrm{dri}}{}^A$.

The calculated values of ΣS_e, $\Gamma_{se}{}^C$ and $\Gamma_{e,\mathrm{dif}}{}^A$ as a function of the current density are shown in Fig. 9(a) for cases 1 and 2. The corresponding electric field at the anode and the anode sheath thickness are shown in Fig. 9(b). One observes that the contribution of the secondary electron flux to the overall electron balance is relatively small compared to the other terms. Thus the difference between $\Gamma_{e,\mathrm{dif}}{}^A$ and ΣS_e is approximately equal to $\Gamma_{e,\mathrm{dri}}{}^A$. The curves representing ΣS_e and $\Gamma_{e,\mathrm{dif}}{}^A$ cross at $\sim j=3200$ mA cm^{-2}, indicating that $\Gamma_{e,\mathrm{dri}}{}^A \approx 0$ at this current density. This is consistent with Fig. 9(b) which shows that at $\sim j=3250$ mA cm^{-2}, both the anode sheath thickness and the electric field at the anode vanish. On the right hand side (i.e., higher current density) of the crossing point, $\Sigma S_e < \Gamma_{e,\mathrm{dif}}{}^A$, and the electron loss to the anode must be constrained by the electric field (drift component of the electron flux is negative). Hence the electric field is directed towards the anode (positive) and an ion anode sheath

is established [Fig. 9(b)]. On the low current density side of the crossing point, $\Sigma S_e > \Gamma_{e,\mathrm{dif}}{}^A$, and the electron loss to the anode must be enhanced by the electric field (drift component of the electron flux is positive). Hence the electric field is directed away from the anode (negative) and an electron anode sheath is established [Fig. 9(b)].

Simulations also suggested that gas heating and the corresponding gas rarefaction contribute to shaping the anode electric field profile. If the equation for gas temperature [Eq. (9)] is not included in the model (a constant 300 K temperature is assumed instead), simulations show the presence of an electron sheath and negative electric field at the anode at $\sim j=3600$ mA cm^{-2}. This is in contrast to case 1, which corresponds to the same current density, and shows an ion sheath and a positive electric field at the anode. Lower gas temperature reduces electron diffusion loss (by decreasing electron diffusivity), and the electric field turns negative to enhance electron drift loss to the anode. The effect of gas temperature on the electron gain and loss rates is rather complicated.[10]

The above discussion suggests that the electric field profile in the anode region, is in fact, determined "*globally*," meaning that the electron gain and loss processes throughout the discharge volume shape the field in the anode region. In contrast, the formation of electric field reversal near the cathode sheath edge depends on the "local" conditions in the cathode fall, mainly the electron diffusion flux emanating from the cathode layer.

In order to further illustrate these phenomena, a simulation (case 3) was performed for a larger electrode spacing ($d=300$ μm), while keeping the same current density as in case 1. The electric field profile reverses twice in the gap [Fig. 10(a)]. The first field reversal occurs at about $l=75$ μm from the cathode where the electric field changes from negative to positive, resembling case 1. In fact, the n_e, T_e, and T_g profiles in the cathode layer were found to be quite similar to those in case 1 [Fig. 10(b)]. Calculations also showed that $j_{e,\mathrm{dif}}/j>1$ at the first reversal point, in agreement with the argument mentioned in connection with Fig. 7. The second field reversal appears further away from the cathode (at $l=185$ μm). The reason for the second field reversal is that the field must become negative near the anode, similar to case 2. This is because $\Sigma S_e > \Gamma_{e,\mathrm{dif}}{}^A$ and the drift flux must become positive to satisfy Eq. (15).

IV. CONCLUSIONS

A one-dimensional self-consistent fluid simulation of a dc microdischarge in He at atmospheric pressure was developed in a one-dimensional parallel plate geometry. The governing equations included mass continuity for charged (e^-, He$^+$ and He$_2^+$) and excited neutral species [He($2\,^3S$), He($2\,^1S$), He($2\,^3P$) and He$_2(a\,^3\Sigma_u^+)$], energy balances to determine the electron and gas temperatures, and Poisson's equation for the electric field.

Atmospheric pressure microdischarges were found to resemble low pressure large-scale dc discharges, underscoring the importance of pd (pressure $\times$ length) scaling. For an interelectrode gap of $d=200$ μm and current density of
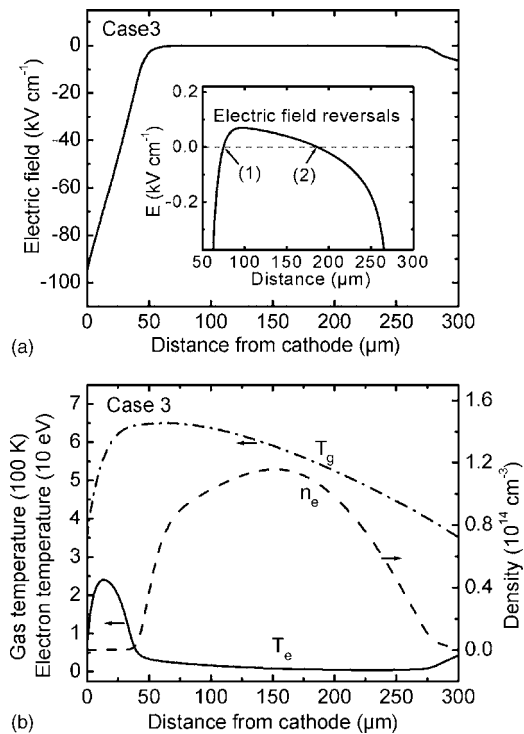
FIG. 10. Plasma properties for the He dc microdischarge of case 3: (a) electric field and (b) gas temperature electron temperature and electron density. The location of electric field reversals in Fig. 10(a) is indicated by arrows.

3600 mA cm⁻², the electric field was found to peak at the cathode and to decay to small values over a distance of ~55 μm from the cathode (sheath edge). The cathode sheath thickness decreased with current density, while the peak electron temperature increased with current density. The electron temperature in the plasma bulk was quite low (≈ 1 eV), and it was insensitive to the discharge current. Atomic ions were the major ionic species in the cathode sheath, while molecular ions were dominant in the bulk. The predicted gas temperatures were between 350 and 600 K, peaking nearer the cathode and increasing with current density (power). Ion Joule heating was found to be the dominant gas heating mechanism.

The simulation predicted the existence of electric field reversals near the cathode sheath edge under the condition of relatively high current density which results in high electron and gas temperatures in the cathode layer. In order to maintain current continuity, electric field reversal becomes necessary when the electron diffusion current emanating from the cathode layer is larger than the discharge current. Similar electric field reversals have been observed in low pressure dc glow discharges.

Depending on operating conditions, the simulation also predicted positive or negative electric field in the anode layer. This was shown to be a "global" effect in the sense that the overall electron density balance controls the behavior of the electric field at the anode. In general, higher discharge current, smaller interelectrode gap, and lower pressure favor the formation of a negative anode potential with respect to the nearby space potential (positive electric field and ion an-

ode sheath). In the opposite case, the anode potential floats above the nearby space potential (negative electric field and electron anode sheath).

Gas heating was found to play an important role in determining the electric field behavior. Higher gas temperature results in smaller gas number density, affecting species transport. As a consequence, the electric field is adjusted to maintain electron current continuity and to preserve the electron density balance. For example, when gas heating was neglected, electric field reversal occurred at higher discharge current density.

ACKNOWLEDGMENTS

[1]K. H. Schoenbach, M. Moselhy, W. Shi and R. Bentley, J. Vac. Sci. Technol. A **21**, 1260 (2003).
[2]M. Moselhy, W. Shi, R. H. Stark, and K. H. Schoenbach, IEEE Trans. Plasma Sci. **30**, 198 (2002).
[3]J. G. Eden, S.-J. Park, N. P. Ostrom, K. -F. Chen, J. Phys. D **38**, 1644 (2005).
[4]M. Miclea, K. Kunze, U. Heitmann, S. Florek, J. Franzke, and K. Niemax, J. Phys. D **38**, 1709 (2005).
[5]F. Iza and J. A. Hopwood, IEEE Trans. Plasma Sci. **31**, 782 (2003).
[6]T. Kikuchi, Y. Hasegawa, and H. Shirai, J. Phys. D **37**, 1537 (2004).
[7]H. Qiu, K. Martus, W. Y. Lee, and K. Becker, Int. J. Mass. Spectrom. **233**, 19 (2004).
[8]D. D. Hsu and D. B. Graves, J. Phys. D **36**, 2898 (2003).
[9]P. S. Kothnur, X. Yuan, and L. L. Raja, Appl. Phys. Lett. **82**, 529 (2003).
[10]M. J. Kushner, J. Appl. Phys. **95**, 846 (2004).
[11]M. J. Kushner, J. Phys. D **38**, 1633 (2005).
[12]Q. Wang, I. Koleva, V. M. Donnelly, and D. J. Economou, J. Phys. D **38**, 1690 (2005).
[13]J. Stevefelt, J. M. Pouvesle, and A. Bouchoule, J. Chem. Phys. **76**, 4006 (1982).
[14]F. Emmert, H. H. Angermann, R. Dux, and H. Langhoff, J. Phys. D **21**, 667 (1988).
[15]D. P. Lymberopoulos and D. J. Economou, J. Appl. Phys. **73**, 3668 (1993).
[16]D. P. Lymberopoulos and D. J. Economou, J. Res. Natl. Inst. Stand. Technol. **100**, 473 (1995).
[17]T. Holstein, Phys. Rev. **83**, 1159 (1951).
[18]J. W. Mills and G. M. Hieftje, Spectrochim. Acta, Part B **39B**, 859 (1984).
[19]A. F. Molisch and B. P. Oehry, *Radiation Trapping in Atomic Vapours* (Oxford University Press, New York, 1998), p. 424.
[20]G. J. M. Hagelaar, G. M. W. Kroesen, U. van Slooten, and H. Schreuders, J. Appl. Phys. **88**, 2252 (2000).
[21]Y. P. Raizer, *Gas Discharge Physics* (Springer-Verlag, Berlin, 1991), pp. 11 and 211.
[22]E. W. McDaniel, *Collision Phenomena in Ionized Gases* (Wiley, New York, 1964), p. 647.
[23]R. Deloche, P. Monchicourt, M. Cheret, and F. Lambert, Phys. Rev. A **13**, 1140 (1976).
[24]L. L. Alves, G. Gousset, and C. M. Ferreira, J. Phys. D **25**, 1713 (1992).
[25]K. A. Berrington, P. G. Burke, L. C. G. Freitas, and A. E. Kingston, J. Phys. B **18**, 4135 (1985).
[26]S. Rauf and M. J. Kushner, J. Appl. Phys. **85**, 3460 (1999).
[27]A. Koymen, F. -C. Tang, X. Zhao, F. B. Dunning,, and G. K. Walters, Chem. Phys. Lett. **168**, 405 (1990).
[28]L. M. Chanin and M. A. Biondi, Phys. Rev. **106**, 473 (1957).
[29]V. K. Saxena and S. C. Saxena, J. Phys. D **1**, 1341 (1968).
[30]E. P. Hammond, K. Mahesh, and P. Moin, J. Comput. Phys. **176**, 402 (2002).
[31]R. A. Gottscho, A. Mitchell, G. R. Scheller, Y. Y. Chan, and D. B. Graves, Phys. Rev. A **40**, 6407 (1989).
[32]J. P. Boeuf and L. C. Pitchford, J. Phys. D **28**, 2083 (1995).